Imaging Stirred-Vessel Macromixing Using Electrical Resistance Tomography

P. J. Holden, M. Wang, and R. Mann
Dept. of Chemical Engineering, UMIST, Manchester M60 1QD, U.K.

F. J. Dickin
Dept. of Electrical Engineering and Electronics, UMIST, Manchester M60 1QD, U.K.

R. B. Edwards
Unilever Research, Port Sunlight Laboratories, Bebington, Wirral L63 3JW, U.K.

An 8-plane 16-sensor ring electrical resistance tomography (ERT) system was designed and installed within a 1.5-m-dia. plant-scale stirred vessel. Results are reported for the unsteady dynamic macromixing of miscible liquids following a pulse addition of brine tracer. Acquired data, after reconstruction, is conveniently represented as a stack of 2-D tomograms and 3-D solid body isosurfaces, thereby providing an equivalent of medical whole-body scanning for a chemical process unit. The results demonstrate the ability of ERT to distinguish the different mixing patterns from two types of impeller in 3-D and to monitor plant-scale miscible liquid mixing processes experimentally, with good resolution in both space and time.

Introduction

After many years of research aimed at the fundamental understanding of "mixing" inside stirred vessels, much of the available theory is still rudimentary and empirical. For nonfacile industrial reactions, selectivity and reactor yield rely upon nonlinear reaction kinetics between species concentrations. In this respect, it is becoming clear that the assumption of perfect backmixing, often automatically and uncritically invoked in semibatch chemical-reactor calculations, is probably almost never the case. This is because industrial reactors have to use reasonably fast reactions to achieve practical productivities. These reaction rates will then most likely be faster than rates of mixing (often minimized to reduce costs), so that spatially uneven concentration fields will develop and reagents will appear partially segregated. Such partial segregation is capable of distorting the product distribution (Mann and El-Hamouz, 1995).

These problems can be tackled by computational fluid mixing (CFM), which is more complex than computational fluid dynamics (CFD), since the complexities of the mixing ensue from the fluid mechanics. Major advances in both CFD and CFM are being driven by constant improvements in available computer power. As a result of these advances, both CFD and CFM now can routinely produce massive amounts of data comprising very detailed predictions of behavior in 3-D space (Ranade et al., 1989; Kresta and Wood, 1991; Bakker and van den Akker, 1994; Mann et al., 1995).

Proper validation of these powerful computer predictions relies upon measurement techniques that furnish a commensurate degree of detail. For example, a typical 3-D stirred-vessel model may comprise 10^5 volume elements. Validation of such a model demands more than a passing corroboration by a handful of pointwise measurements.

Laser Doppler anemometry (LDA) has been successfully deployed for validating CFD predictions, although the gathering of sufficient spatial data needs laborious repeated acquisition throughout the vessel 3-D space (Wu and Patterson, 1989; Bakker and van den Akker, 1994). Digital particle image velocimetry (DPIV) is a later development requiring less onerous repetitive acquisition (Armenante and Chou, 1996). However, both these approaches focus on local average and turbulent velocity fluctuations and thus do not address issues of rates of mixing.

Electrical resistance tomography (ERT), on the other hand, is capable of noninvasively measuring time-evolving concentration fields, hence mixing rates, within a stirred vessel to a spatial resolution approaching 10^4 volume elements or voxels

Correspondence concerning this article should be addressed to R. Mann.

(Mann et al., 1997). Moreover, this electrically based tomographic approach offers timewise resolution of the order of 10^{-1} s and is thus ideally suited for typical mixing assessment and validation against CFM predictions.

This article describes an application of a plant-scale 8-plane ERT system with 16 radial sensing elements in each plane. Reconstructed macromixing concentration fields can be compactly presented as solid-body isosurfaces in 3-D. Such solid-body graphics of internal mixing for a stirred vessel are somewhat equivalent to whole-body CAT scanning as used in medicine.

Electrical Resistance Tomography

Some five years ago, UMIST constructed an ERT data-acquisition system (DAS) (Wang et al., 1993; Dickin and Wang, 1995) for application of ERT to miscible single-phase fluid mixing in a laboratory stirred vessel (McKee et al., 1994). However, to apply the technique to mixing at plant scale, the DAS and sensor system should be extended to acquire 3-D data at faster rates (down to milliseconds). A 2.7-m^3 plant-scale vessel made of polypropylene was installed in the UMIST pilot plant. The 3-D sensor system and the DAS used for monitoring mixing within this vessel were designed, evaluated, and configured for demonstrating plant-scale feasibility and understanding the fundamentals of scaling up mixing processes in stirred vessels (Mann et al., 1996). A qualitative image reconstruction algorithm has been used for this initial study.

Sensing system

The goal of electrical resistance tomography is to obtain the resistance distribution in the domain of interest. The resistance distribution in a cross section can be obtained by injecting currents (or applying voltages) on the domain and measuring voltages (or current) on it via a number of spaced electrodes that are mounted noninvasively on its boundary. There are several sensing strategies to obtain the resistance distribution. A measurement protocol, known as the Adjacent Electrode Pair strategy (Barber et al., 1983), has been adopted (Figure 1), which is based on injecting current using a pair of neighboring electrodes and measuring the voltage differences, using all other pairs of neighboring electrodes. This process is then repeated by injecting current using all other possible pairs of neighboring electrodes.

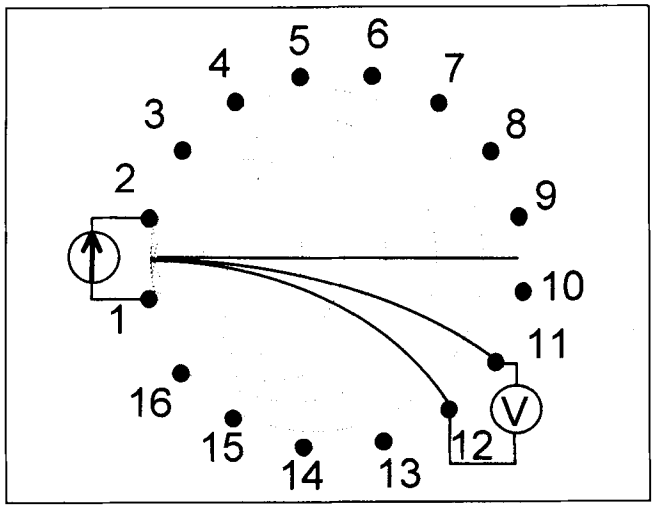

Figure 1. Adjacent electrode-pair sensing strategy (equipotential lines, solid; current streamlines, dotted).

To obtain a 3-D field distribution, an 8-plane assembly of sensing rings, each containing 16 electrodes, has been designed and constructed for the 2.7-m^3 plant-scale stirred vessel of principal dimension 1.5 m used in the study (Mann et al., 1996; Wang et al., 1996). This sensor system is shown in Figure 2. The dimensions and spacing of the eight planes, numbered from the top downward, are indicated in Figure 2a. Figure 2b shows a photographic view of the vessel interior with an A310 impeller in place. Some seven vertical rows of the electrode rectangular sensing plates can be seen. The ex-

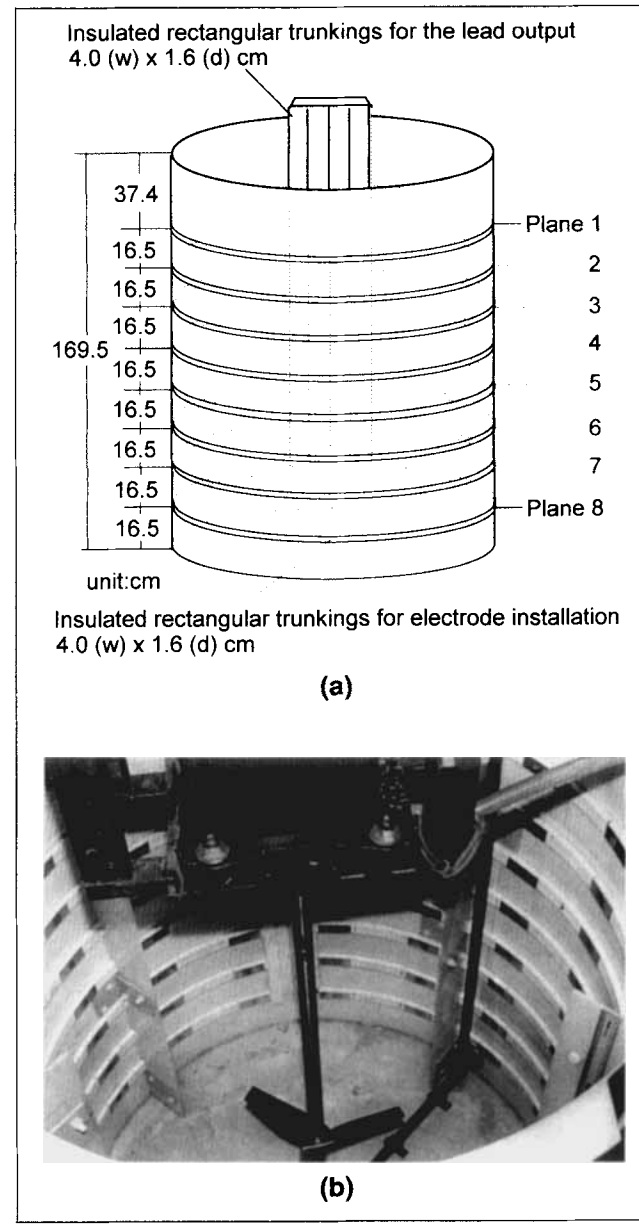

Figure 2. (a) Sensor system dimensions; (b) interior view of the UMIST vessel.

treme righthand row has the plates for all eight rings visible. The impeller is positioned at a clearance of one-half above the base, adjacent to sensor plane 5.

Data-acquisition system

An accurate and stable DAS is a basic necessity and incorporates signal sources, an electrode multiplex array, voltmeters, signal demodulators, and a system controller. Such complexity is necessary due to the low amplitude of measurement at the boundary that are of the order of mV; the small responses of the dynamic change that are of the order of μV; the large number of electrode channel operations (a minimum of 832 for the 8-plane 16-electrode ring-sensor system); the high common voltages that are of the order of V; and the large stray capacitance of coaxial cable (of which more than 300 m is needed for the associated cabling).

The original UMIST Mk.1b acquisition system (Wang et al., 1993) has been upgraded and is made up of six functional parts, as shown in Figure 3. The main specifications of the enhanced DAS are: frequency, 75–153.6 kHz; current range, 0–50 mA (pk–pk); frame speed, 40 ms; voltmeter sensitivity, 0.0488 μV; driving capacitance capability, 1000 pF (cable length 10 m each channel); electrode number, 128; sensor excitation and measurement strategy software, flexible.

Image reconstruction

In order to determine the internal distribution of conductivity within the process vessel from measurements acquired from an array of electrodes mounted on its periphery, an image reconstruction algorithm is initially used. The algorithm supplied with the Mk.1b system resides in the host computer connected to the data-acquisition system and can be used to reconstruct both on- and off-line. The algorithm used here is often referred to as a "qualitative" algorithm, as the images depict relative change in resistivity against an initially acquired set of reference data. The reference data are usually acquired prior to the start of the experiment under quiescent conditions.

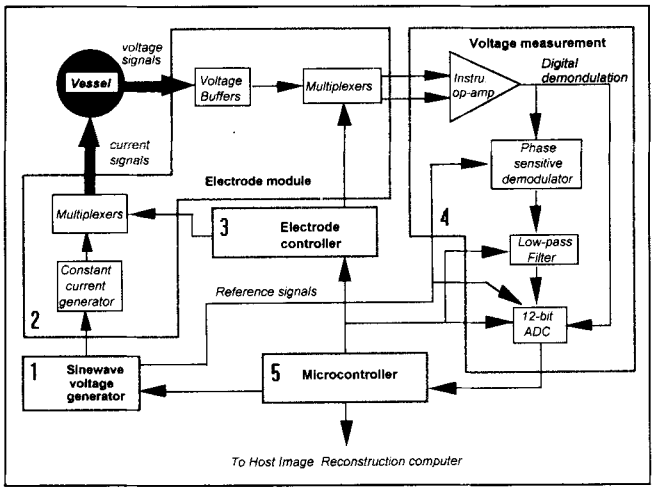

Figure 3. Structure of the UMIST Mk 1b data-acquisition system.

The qualitative algorithm initially used for the study (Wang et al., 1996), as shown in Eq. 1, is more formally known as a linear back-projection (LBP) method utilizing a sensitivity-coefficient weighting method first defined by Geselowitz (1971) and later refined for ERT by Kotre (1989). The main advantage of this algorithm is that it can be performed in a single step using a precalculated pixel sensitivity matrix that is stored in the computer's memory. The image is simply reconstructed by a matrix/vector multiplication operation that can be performed rapidly on modern computers equipped with floating-point units. Thus:

$$[P(\sigma_m)]_M = \sigma_0/(([K]_{M,N})\cdot[\eta]_N), \tag{1}$$

where the conductivity relative value, σ_m, at pixel m is represented by a column matrix, P; $[\eta]_N$ represents the relative value of boundary measurements; M is the number of pixels; N is the number of boundary measurements; and σ_0 is the conductivity for a homogeneous case for the reference measurement. The entry of the normalized sensitivity matrix $[K]_{M,N}$ is given by Eq. 2 using the sensitivity coefficients adopted from Kotre's method:

$$K_{m,n} = S_{m,n} \Big/ \sum_{n=1}^{N} S_{m,n}. \tag{2}$$

However, the accuracy of the imaging data from the 2-D presumption is limited somewhat due to both the 3-D distribution of real electric fields and the LBP algorithm. A "full" 3-D electrical resistance tomographic analysis is being developed at UMIST to overcome the inherent problems of this 2-D algorithm (Pinheiro et al., 1997). More complete details of the preceding qualitative reconstruction method are available (Mann et al., 1996).

Finally, it should be noted that in order to confine the tomographic images to the effects of internal vessel mixing, the impeller and baffles are incorporated into a base-line measure of each plane's conductivity. This subtracts their input from changes in fluid conductivity. The impeller rotation has a negligible effect on this fluid conductivity background.

Development on a Plant-Scale Vessel

Phantom detection

In order to test the sensitivity and spatial resolution of the ERT system, a number of phantom detection experiments were performed with aluminum and PVC cylinders, which provide a marked contrast in conductivity. The voltage measurement data were reconstructed using the modified sensitivity coefficient algorithm to produce a 2-D image of the corresponding relative changes in conductivity distribution inside the vessel.

Figure 4 shows the reconstructed image for plane one, for three cylinders (a 11-cm aluminum, 6-cm aluminum, and 11-cm PVC) inserted into the vessel to a depth of 20 cm below the liquid surface. Each of the three cylinders were placed 15 cm from the wall of the vessel midway between the baffles, with the PVC cylinder in the topmost quadrant, the 11-cm aluminum one in the "right" quadrant and the 6-cm aluminum in the "left" quadrant (positions as shown in Figure 4). The resultant reconstructed image clearly discriminates all

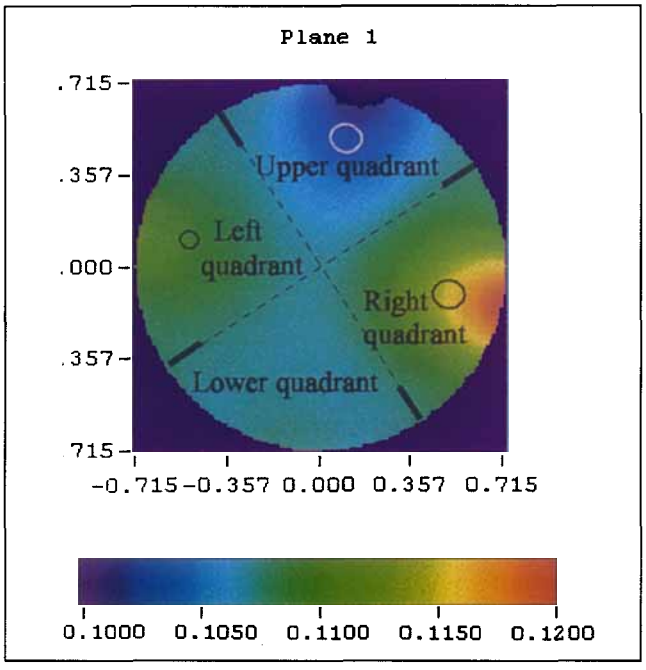

Figure 4. Phantom detection, 11-cm aluminum, 6-cm aluminum, and 11-cm PVC cylinders.

three "phantom" objects (PVC appearing blue as a region of lower conductivity than the background, aluminum red/yellow as a region of higher conductivity), although the centers of their predicted locations appear to be slightly closer to the tank wall. From these results it can be deduced that the spatial resolution of the system is approximately of the order of 4.2% of the vessel diameter. The small discrepancy in phantom position is indicative of sensitivity effects of the reconstruction algorithm and the electric current injection protocol used. The small 6-cm aluminum cylinder is only just detectable on reconstruction, thus establishing the limit of spatial resolution for a high-conductivity object. The limits of spatial resolution do, however, depend on the conductivity contrast.

Swirl and baffle effects

When a fluid is agitated in a stirred vessel without baffles, an air–core vortex is formed around the impeller shaft due to the swirling motion of fluid induced by the impeller. At high agitator speeds, even with baffles, a small intermittently unstable vortex is inevitably encountered around the agitator shaft, and in addition, small intermittent vortices form and disappear around the baffles.

Figure 5 shows photographs taken around the impeller

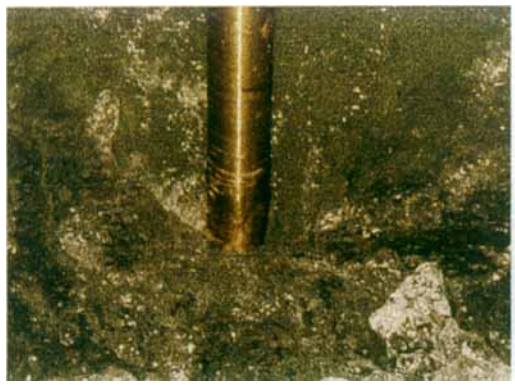

Vortex around impeller shaft

Baffle Effect

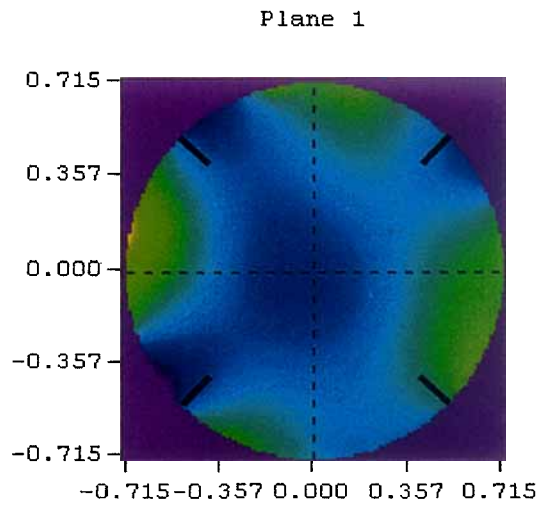

Figure 5. Swirl and baffle effects.

shaft and baffles when water was agitated using a Rushton disk turbine at a high stirrer speed of 200 rpm. A vortex around the impeller shaft and swirl effects around the baffles can be clearly seen. From the reconstructed tomogram at the topmost plane in the same figure, a low conductivity region is indicated around the impeller shaft and behind three of the baffles. As the conductivity of the fluid has not changed, it seems reasonable to assume that these low-conductivity regions are due to local bubble induction by the central vortex and baffle swirl effects.

Miscible liquid mixing: Brine tracer pulse tests

As resistance tomography can detect local changes in conductivity/resistivity, the technique can be used to study the unsteady mixing dynamics of miscible liquids if the fluids to be blended have differing conductivities. A simple test involves injecting a small quantity of strong brine solution into water and reconstructing the resistivity field from the peripheral sensors at each axial plane.

Two experiments were performed to examine the ability of the ERT system to distinguish between differing flow patterns, as the tracer is dispersed, through interpretation of the reconstructed images. The first experiment used a Rushton disk turbine impeller that generates a predominantly radial flow, the second used a Lightnin A310 that produces an axial flow that generates a single large-circulation loop over the height of the vessel.

Results are presented at various time increments following the surface addition of 1 dm^3 of concentrated brine solution (conductivity 15.0 mS/cm) into domestic tap water (conductivity 0.11 mS/cm) at $t = 0$. For both impellers stirring was at the lowest speed of 75 rpm, which gives Reynolds numbers greater than 100,000. At this lowest speed, stirrer and baffle vortex effects were negligible and do not therefore complicate the mixing images obtained.

Figures 6 (Rushton disk turbine) and 7 (Lightnin A310) show typical data sets of resistivity contours from the eight axial planes represented as a "stack" of tomograms. High conductivity appears red and low conductivity regions are blue, separated by intermediate levels of yellow/green for intermediate concentrations. Figures 8 and 9 show the same experimental tests but the eight planes are now rendered as solid-body isometric and overhead plan view images. In the solid-body images conductivity at the outermost isosurface is 95% of the final fully mixed conductivity. Thus, the conductivity is less than 0.115 mS/cm for the clear outer apparently hollow space and greater than 0.115 mS/cm within the solid body. In this way, the clear portion of the figures shows the extent to which the fluid volume remains unmixed below the final uniformity. This 95% approach to being fully mixed is often used to define a practical "mixing time."

Rushton disk turbine

On examining Figures 6 and 8 together, the qualitative spatial distribution of salt concentration is readily discernible. After 2 s, the concentrated brine plume has convected downward and reached plane three. It is worth noting here that the tomogram at plane one, just below the injection position, appears to, strangely, show a moderately low conductivity region, when theoretically the highest conductivity should be encountered. In fact, it appears that the concentrated solution occurs in such a small volume that it is momentarily below the spatial resolution of the ERT system. After a further 2 s, the brine "cloud" has enlarged and reached the impeller and is being dispersed and discharged out toward the tank walls by the strong radial outflow in this region. Furthermore, the tracer is being swept in a clockwise sense by the locally strong swirl flow around the impeller. This swirl flow seems significantly stronger than can be seen above (planes 1, 2, 3) and below (planes 6, 7, 8) the impeller envelope.

After 6 s, regions of high conductivity appear at the tank wall in all eight planes, suggesting that the tracer has begun to recirculate in the axial sense both up and down the tank walls, although from the solid-body-plan view, the moderately concentrated brine occurs mainly in one quadrant, showing the slow rate of tangential mixing from the surface addition. After a further 2 s, more of the brine has dispersed and swirled in both the lower and upper parts of the vessel. Again the upper half of the vessel shows significant concentration differences, although the high conductivity region has decreased compared with the previous image.

The remainder of the time sequence shows the somewhat slow approach toward the final fully mixed condition, at $t \approx 18$ s, which appears controlled by the slower rate of tangential mixing. It is interesting to note that even after 14 s, the ERT system can detect patches of low conductivity corresponding to regions of low salt concentration. After 18 s, the solid body image shows the whole of the vessel to be within 95% of the final conductivity, except for a small region of low conductivity at the center of the uppermost plane. It may be that this is caused by the presence of a small intermittent vortex, as previously discussed.

Finally, it needs to be emphasized why, for instance, the top plane one view in Figure 6 after 18 s appears different from the solid-body image in Figure 8 at the same instant. The experimental concentration field in 3-D is, in fact, exactly the same in both cases. However, the two methods of presentation make them seem different. In Figure 6 the concentration differences are shown by color gradation, with the color differences operative over the whole range of concentrations. In Figure 8, the solid-body rendering exposes contour lines that delineate regions of differing concentration. These show up especially prominently in the overhead plan views. Moreover, Figure 8 uses a truncated range with a nonfilled (clear) invisible representation for that part of the fluid that has a concentration lower than 0.95 of the final fully mixed condition. This creates a solid-body image that is intelligible in a different way, intended to emphasize more graphically departures from final perfect mixedness.

Lightnin A310

Examining Figures 7 and 9 together, after 2 s, the tomographic images show clearly the changes in local resistivity, down to plane three, arising from a surface pulse of the more concentrated brine solution. At 4 s, the concentrated brine slug has dispersed "outwards" in a radial sense, but downward axial dispersion appears inhibited by the outer up-flowing fluid generated by the downward "pumping" impeller. After a further 2 s, regions of high conductivity are noted at

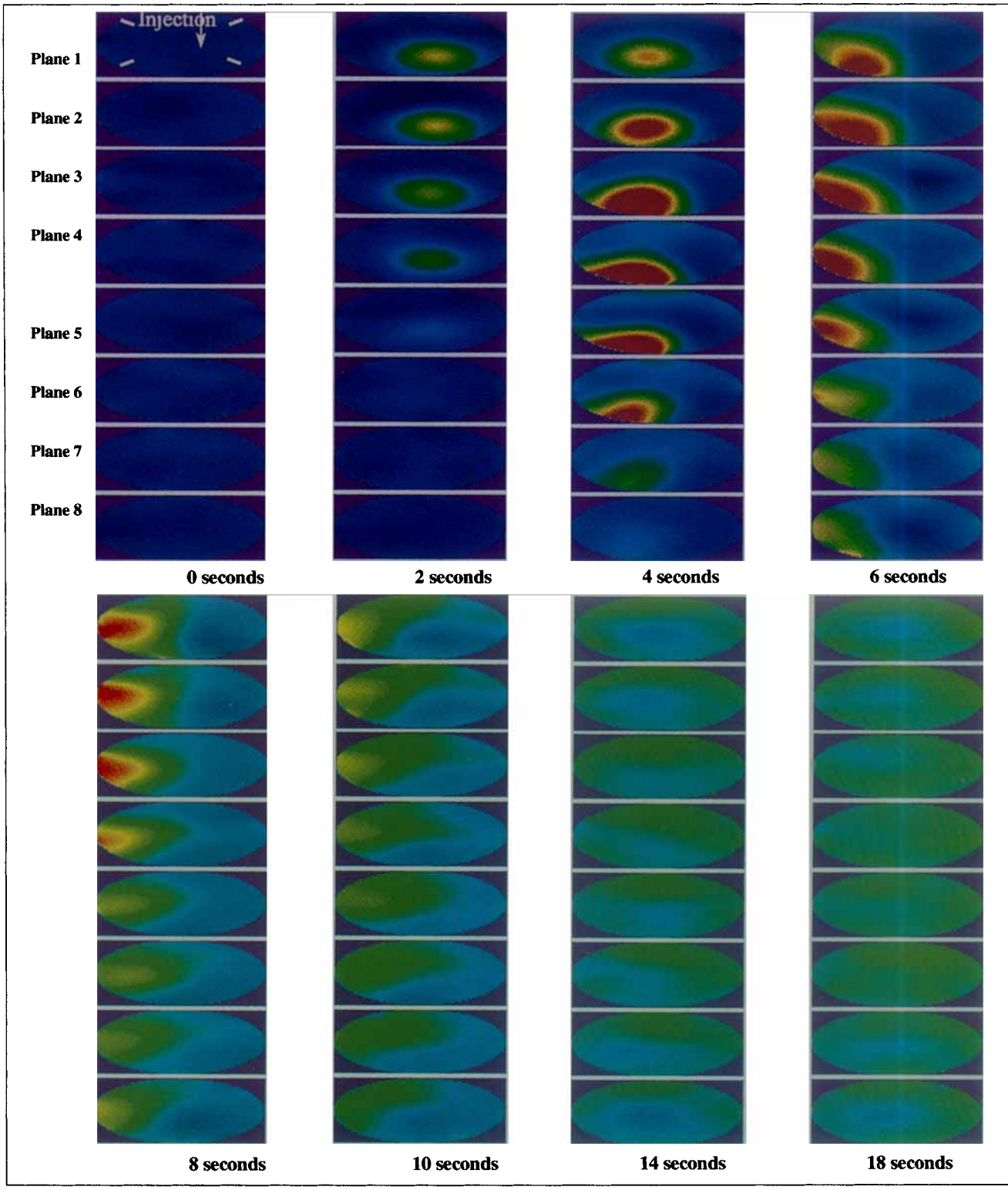

Figure 6. Stack of tomograms following a pulse injection of high-conductivity salt solution into domestic tap water, Rushton turbine 75 rpm.

the walls, and tangential dispersion is observed into the second quadrant. Again most of the high concentrations appear in the upper third of the vessel.

Viewing the solid-body reconstruction at 10 s, the brine appears to have reached the impeller position and been dispersed through the impeller into the opposite half of the vessel, forced downward and out radially in a "cork-screw" motion as a result of the maximum axial and tangential fluid velocities around the impeller tip. The tangential dispersion now seems quite significant, with the high-conductivity solu-

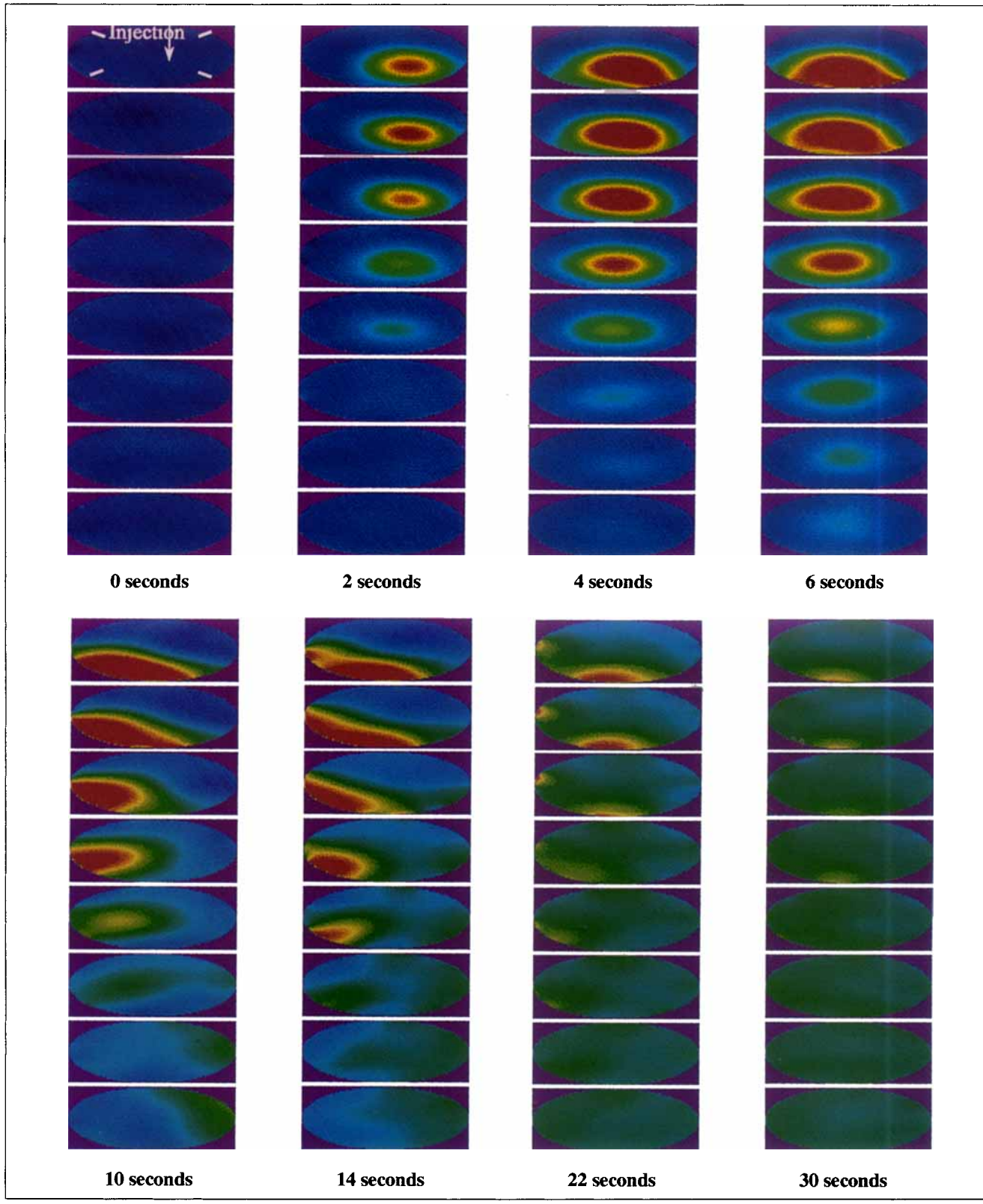

Figure 7. Stack of tomograms following a pulse injection of high-conductivity salt solution into domestic tap water, Lightnin A310, 75 rpm.

tion appearing closer to the wall. The high-conductivity area close to the impeller shaft has been dispersed by the axial downward convection at this position.

After 14 s, Figures 7 and 9 show that in the lowest planes, 7 and 8, brine is present at an apparently almost uniform concentration (more green than blue), with only slight varia-

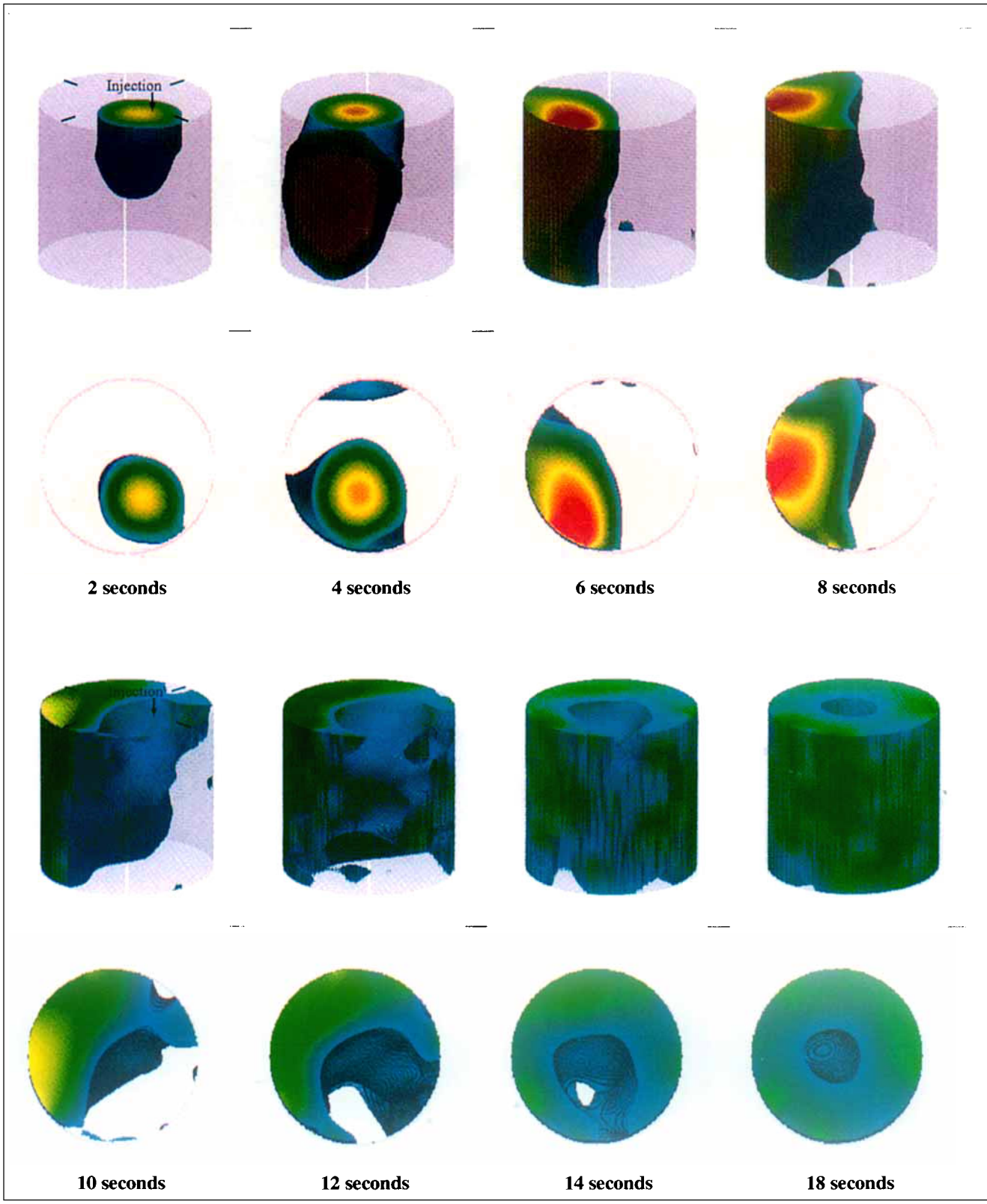

Figure 8. Solid-body surface following a pulse injection of high-conductivity salt solution into domestic tap water, Rushton turbine 75 rpm.

tions across each of these two planes. However, in the left quadrant, the upper planes, 5 up to 1, still show a high concentration of brine (red), which is maximum at plane 2, and large concentration gradients still exist across these five planes. Figure 7 indicates that at 14 s, the A310 impeller has provided relatively slow tangential/circumferential mixing

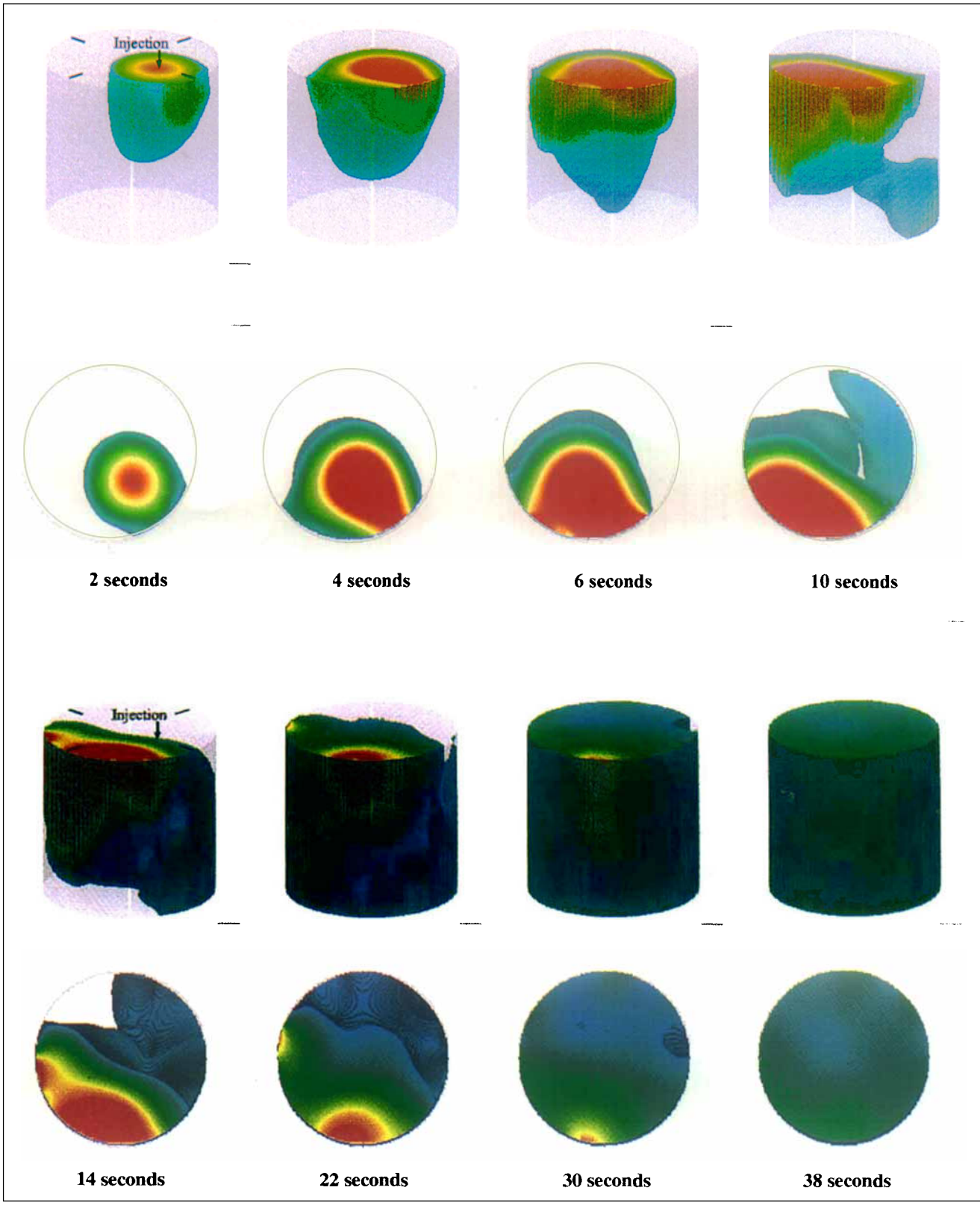

Figure 9. Solid-body surface following a pulse injection of high-conductivity salt solution into domestic tap water, Lightnin A310, 75 rpm.

rates. Thus while there is axial top-to-bottom mixing, it is not uniform across the radial planes. This shows up clearly in Figure 9, especially the upper isometric perspective view, where the solid-body representation emphasizes that brine has been mixed across the central axial region from top to bottom, but low brine "clear voids" exist in the rear and

righthand top-plane quadrants and in the lowest plane front quadrant.

After a further 8 s, the brine has become more uniform across the whole of the lower half of the vessel, with some slight nonuniformity still persisting at planes 1, 2, and 3 in Figure 7. The images at 30 s then show the vessel very close to the fully mixed condition, while after 38 s, both the isometric and overhead solid-body views in Figure 9 show complete uniformity.

Finally, by comparing the solid-body images in Figures 8 and 9, it is evident that the ERT system can detect and represent some quite striking visual differences in the mixing patterns generated by the two types of impeller.

Pointwise measurements and mixing curves

While the previous figures depict an overall qualitative description of the mixing process, it is sometimes useful to consider local pointwise values and present them in a form equivalent to a mixing curve. Using the reconstructed tomographic data, it is possible to construct mixing-time curves at any pixel location (from a total of 316×8) from any of the eight imaging planes. The set of pixels are based on a square mesh of size 20×20 with some 316 of the 400 total lying inside each circular plane. Each pixel is thus 71.5×71.5 mm for the 1.43-m-diameter vessel. As an illustration, two spatial positions were selected from the Lightnin A310 experiment and the deduced mixing-time curves are plotted for four of the eight imaging planes. Position one corresponds to the surface addition point and position two is rotated 90° (in the direction of rotation) from the addition point at a pixel midway between the impeller shaft and the tank wall.

Considering the curve at plane one, position 1 (Figure 10a), the concentration rises to a maximum value at $t \simeq 3$ s before decreasing to a minimum value at $t \simeq 12$ s. Thereafter the curve "blends" upward from the relatively low value to the final fully mixed condition. This pattern is observed for the other axial positions above the impeller, although the peak magnitude is decreased with increasing downward distance from the injection position. Examining the curves below the impeller for planes 6 and 8 (Figure 10a), distinct differences are noticeable. These mixing curves rise slowly to a peak at $t \simeq 8$ s lower then the fully mixed condition, before initially decreasing and then finally rising to the final mixed condition. These phenomena also confirm the previously observed slower rate of axial mixing below the impeller.

At position 2 (Figure 10b) similar initial trends are observed for planes 1 and 3 above the impeller, but for plane 6 below the impeller, the dimensionless concentration rises above 1.0 to a maximum, although there is some delay in reaching this value because of the increased distance from the injection position. However, the mixing curves do not now decrease to a minimum, but gradually descend to the final condition over a longer period of approximately 30 s. Similar trends are observed for the lowest plane, 8, below the impeller, although the concentration at this lowest plane never rises above the final condition.

It is observed from both Figures 10a and 10b that the predicted mixing time depends on the location of the detection point, although variations of concentration deviations from the final mean value are very small for both positions after

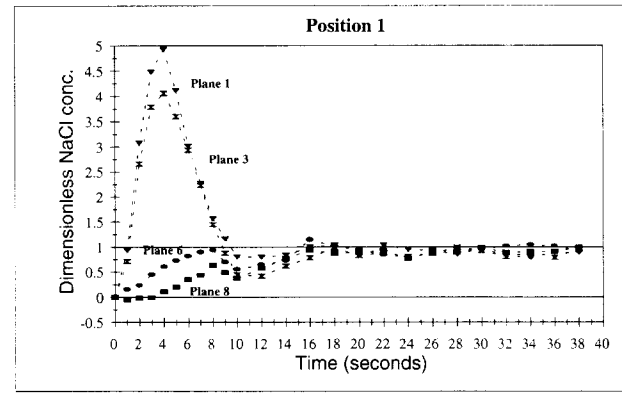

(a)

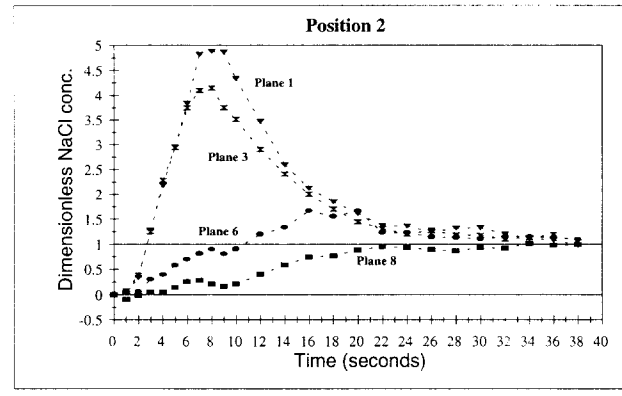

(b)

Figure 10. (a) ERT mixing-time curve, Lightnin A310, 75 rpm, position 1; (b) ERT mixing-time curve, Lightnin A310 75 rpm, position 2.

approximately 25 s. The mixing time is shown to be between 25 and 35 s, depending on the stipulated degree of approach to final uniformity.

Conclusions

1. A large-scale electrical resistance tomography system has been successfully constructed in a 2.7-m^3 vessel using an 8-plane set of peripheral sensing rings, each containing 16 electrodes. The 3-D electrical resistance distribution can be measured within 0.3 s for the full set of eight tomograms using an adjacent current-injection protocol.

2. Acquired peripheral conductivity data, after reconstruction, can conveniently represent dynamic mixing behavior as a stack of 2-D tomograms or as 3-D solid-body isosurfaces, thereby providing an equivalent of medical whole-body scanning for a chemical process unit. The spatial resolution is of the order of 5%, using 16 equispaced electrodes. This was confirmed by phantom detection tests. Increasing the number of electrodes would improve the spatial resolution, although there are intrinsic mathematical limits to this spatial detectability.

3. The ability of the system to distinguish different flow patterns from two types of impeller in 3-D and to monitor mixing processes at plant scale has been demonstrated by monitoring the dispersion of a brine pulse tracer.

4. Pointwise mixing curves can be readily constructed from any pixel in any one of the eight imaging planes, thus giving a quantitative description of the local mixing rates, subject to sensitivity errors in the reconstruction algorithm.

Acknowledgments

The authors gratefully acknowledge the support of the EPSRC for Grant GR/J 50798 and a studentship for P. J. Holden. Additional financial support was also provided by Unilever Research.

Literature Cited

Armenante, P. M., and C. Chou, "Velocity Profiles in a Baffled Vessel with Single or Double Pitched-Blade Turbines," *AIChE J.*, **42**, 42 (1996).

Bakker, A., and H. E. A. van den Akker, "Single Phase Flow in Stirred Reactors," *Trans. Inst. Chem. Eng.*, **72**(A), 583 (1994).

Barber, C. D., B. H. Brown, and I. L. Freeston, "Imaging Spatial Distributions of Resistivity Using Applied Potential Tomography," *Electron Lett.*, **19**, 933 (1983).

Dickin, F. J., and M. Wang, "Impedance Sensors—Conducting Systems," *Process Tomograpy*, Chap. 5, R. A. Williams and M. S. Beck, eds., Butterworth-Heinemann, Stoneham, MA, p. 63 (1995).

Geselowitz, D. B., "An Application of Electrocardiographic Lead Theory to Impedance Plethysmography," *IEEE Trans. Biomed. Eng.*, **BME-18**, 38 (1971).

Kotre, C. J., "A Sensitivity Coefficient Method for the Reconstruction of Electrical Impedance Tomograms," *Clin. Phys. Physiol. Meas.*, **10**(3), 275 (1989).

Kresta, S., and P. E. Wood, "Prediction of Three-Dimensional Turbulent Flow in Stirred Tanks," *AIChE J.*, **37**, 448 (1991).

Mann, R., F. J. Dickin, T. Dyakowski, R. A. Williams, R. B. Edwards, A. E. Forrest, and P. J. Holden, "Application of Electrical Resistance Tomography to Interrogate Mixing Processes at Plant Scale," *Chem. Eng. Sci.*, **52**, 2073 (1997).

Mann, R., and A. M. El-Hamouz, "Paradoxical Product Distributions on Scaling-Up a Stirred Batch Reactor," *AIChE J.*, **42**, 855 (1995).

Mann, R., S. K. Pillai, A. M. El-Hamouz, P. Ying, A. Togatorop, and R. B. Edwards, "Computational Fluid Mixing for Stirred Vessels: Progress from Seeing to Believing," *Chem. Eng. J.*, **59**, 39 (1995).

Mann, R., M. Wang, F. J. Dickin, T. Dyakowski, P. J. Holden, A. E. Forrest, and R. B. Edwards, "Resistance Tomography Imaging of Stirred Vessel Mixing at Plant Scale," *Inst. Chem. Eng. Symp. Ser.*, **140**, 155 (1996).

McKee, S. L., R. A. Williams, and A. Boxman, "Development of Solid-Liquid Mixing Models Using Tomographic Techniques," *Process Tomography—A Strategy for Industrial Exploitation*, M. S. Beck, E. Campogrande, E. Hammer, M. A. Morris, R. A. Williams, and R. C. Waterfall, eds., UMIST, Manchester, UK, p. 342 (1994).

Pinheiro, P. A. T., W. W. Loh, M. Wang, R. Mann, A. E. Forrest, and F. J. Dickin, "Three-Dimensional Electrical Resistance Tomography in a Stirred Mixing Vessel," *Frontiers in Industrial Process Tomography: II*, Delft, The Netherlands, p. 251 (1997).

Ranade, V. V., and J. B. Joshi, "Flow Generated by Pitched Blade Turbine I: Measurements Using Laser Doppler Anemometer," *Chem. Eng. Commun.*, **81**, 197 (1989).

"Spyglass Slicer: Quick Tour and Reference," Spyglass, Inc., Champaign, IL (1994).

Wang, M., F. J. Dickin, and M. S. Beck, "Improved Electrical Impedance Tomography Data Collection System and Measurement Protocols," *Tomography Techniques for Process Design and Operation*, M. S. Beck, E. Campogrande, M. A. Morris, R. A. Williams, and R. C. Waterfall, eds., Computational Mechanics Publications, Southampton, U.K., p. 65 (1993).

Wang, M., R. Mann, F. J. Dickin, and T. Dyakowski, "Large-Scale Electrical Tomography Sensing System to Study Mixing Phenomena," Int. Workshop on Image and Signal Processing Advances in Computational Intelligence, Manchester, UK (1996).

Wu, H., and G. K. Patterson, "Laser-Doppler Measurements of Turbulent-Flow Parameters in a Stirred Mixer," *Chem. Eng. Sci.*, **44**, 2207 (1989).

Manuscript received Mar. 21, 1997, and revision received Nov. 20, 1997.